Computers & Fluids, Volume 39, Issue 5, May 2010, Pages 756–767

INVESTIGATION OF THE INFLUENCE OF SWIRL ON A CONFINED COANNULAR SWIRL JET

K.K.J.Ranga Dinesh [1], M.P.Kirkpatrick [2], K.W.Jenkins [1]

1. School of Engineering, Cranfield University, Cranfield, Bedford, MK43 0AL, UK.

2. School of Aerospace, Mechanical and Mechatronic Engineering, The University of Sydney, NSW 2006, Australia.

Corresponding author: Ranga.Dinesh@Cranfield.ac.uk

Telephone: +44 (0) 1234 750111 ext 5350

Revised Manuscript prepared for the Journal of Computers and Fluids

22nd July 2009

ABSTRACT

Large Eddy Simulations are used to model a turbulent confined coannular combustor and examine the effects of swirl on the flow field and mixing. Three separate simulations with relatively high mesh resolutions and different swirl numbers have been carried out using a finite volume method on a Cartesian non-uniform structured grid. A localised dynamic Smagorinsky model is used to parameterize the subgrid scale turbulence. The snapshots of the axial and swirl velocities and velocity vector fields show the complex flow patterns developing with increased swirl number and the rapid decay of axial momentum. Precessing vortex cores (PVC) were identified for all three cases and the mean axial velocity plots indicate that the upstream extremity of the vortex breakdown bubble shifts towards the inlet as the swirl number increases. The calculated power spectra indicate the distinct precession frequency for high swirl number. The probability density functions of axial velocity showed the changes of their distributions from Gaussian to non-Gaussian with increased swirl number. The swirl affect is larger for the axial velocity decay all through the domain and only affect largely for the swirl velocity decay at near field. The correlation between swirl number and the axial extent of the recirculation zone is approximately linear. The radial plots of mean passive scalar and its variance also demonstrate an increase in the rate of mixing with increasing swirl number.

Key Words: Large eddy simulation, Swirl, PVC, Precession frequency, Vortex breakdown, Scalar mixing

1. INTRODUCTION

Swirl is important in many practical flows. Understanding the characteristics of swirl for various conditions still remains a major focus in fluid dynamics research because of its relevance to various types of engineering applications. Swirl is used in many applications to improve mixing because it can form an adverse pressure gradient which can provide an aerodynamic barrier to the flow. Swirl can create different flow patterns such as vortex breakdown (VB) induced recirculation and coherent structures known as “precessing vortex cores” (PVC). Although the swirl and its applications have been exploited for some time, a comprehensive understanding of the nature of swirl remains an elusive goal, especially in combustion applications where the interaction between combustion dynamics and swirling shear layers, turbulence-chemistry interactions under different swirl strengths. Also, the effects of swirl on global flame extinction known as lean blowout (LBO) which can lead to combustion instability and the structure of the droplet vaporisation with swirl in spray combustion systems remain poorly understood. As described by Lieuwen and Yang [1] and Syred [2] investigations of flow features associated with combustion are much more expensive and challenging than isothermal flows. As the current combustion systems in industry are moving towards lean burn combustion, the topics of combustion instability associated with swirl have received increasing attention. The introduction of swirl can induce high shear rates and strong turbulence intensities which can lead to inhomogeneity particularly in heat release patterns, which may lead to combustion instabilities. The task of collecting the information required to improve our overall

understanding is far from complete and more research on swirl stabilised systems is required.

To date a multitude of theoretical and experimental studies have been undertaken and have addressed many factors from the fundamental to the design level. For example, Squire [3], Randall and Leibovich [4], Krisbus and Leibovich [5] described VB phenomena using different mathematical expressions under various conditions. Various experimental configurations have also been used to investigate swirl based flow patterns especially in combustion applications. For example, Chanaud [6] investigated the effect of swirl on flame stability. Froud et al. [7] studied the coupling phenomena between flow dynamics, combustion and acoustic waves which can lead to thermoacoustic instabilities.

Computational studies can offer useful details of the unsteady behaviour in complex configurations involving swirl. Direct numerical simulation (DNS), in which all scales of motion are resolved, is possible, but only at Reynolds numbers well below the range of engineering importance. On the other hand, large eddy simulation (LES), in which only the large scale motions are resolved and the effect of small scales is modelled, can now be performed at such Reynolds numbers as are found in practical engineering systems. The development of the LES technique over the past ten years and developing computing resources has permitted the prediction of swirl flows in complex engineering configurations and the validation of the predictions against a range of experimental data sets. Earliest investigations using LES of swirl stabilised coannular combustor were done independently by Pierce and Moin [8] and Kim et al. [9]. Grinstein et al. [10] also studied the flow field around a fuel injector nozzle using a monotone integrated large eddy simulation (MILES) method. A LES technique with

Lagrangian particle tracking was first applied by Apte et al. [11] for particle laden swirling flow. Lu et. al. [12] conducted LES of swirling flow in a dump combustor and James et al. [13] studied the flow dynamics of one of the Rolls-Royce aero engine combustors using LES. Wegner et al. [14] also carried out LES of a generic type combustor and Wang et al. [15] conducted LES of a gas turbine swirl injector.

LES has also been applied to model swirl combustion applications for various flow and flame conditions. Pierce and Moin [16] simulated swirling flames and studied the flame dynamics in a coannular combustor. Di Mare et al. [17] performed LES of a model gas turbine combustor and Mahesh et al. [18] investigated a section of the Pratt and Whitney gas turbine combustor using LES. Bioleau et al. [19] used LES to study the ignition sequence in an annular chamber and demonstrated the variability of ignition for different combustor sectors and Boudier et al. [20] studied the effects of mesh resolution for LES of complex geometry encountered in gas turbine combustors. Roux et al. [21] performed LES of isothermal and reacting flows in a simplified ramjet combustor and analysed the combustion instabilities. Very few attempts have been made so far for LES of spray combustion in swirl based applications. For example, Sankaran and Menon [22] carried out LES of non-premixed spray flames and Reveillon and Vervisch [23] demonstrated spray vaporisation in non-premixed flames with a single droplet model. Patel and Menon [24] studied the interactions between spray, turbulence and flame in a lean premixed combustor.

Despite the various investigations and key points addressed in the literature, the dynamical nature of swirl based engineering applications is still not well understood, especially over a wide range of more practically oriented conditions. Experimental

investigation of the complete unsteady nature of swirl based engineering systems is especially challenging and expensive. Therefore accurate simulations can overcome some difficulties that arise in experimental studies and uncover more details of the unsteady nature in swirl based configurations once the calculations have been validated with available experimental data. The influence of swirl on flow field and mixing is an important topic especially for the combustor type geometries and hence accurate and reliable prediction in such situations using state-of-art numerical techniques is of considerable interest. With this in mind, the present paper investigates the influence of swirl on the flow field and mixing in a coannular swirl combustor using large eddy simulation (LES).

The configuration considered for this study is a confined coannular swirl combustor experimentally investigated by Sommerfeld and Qiu [25][26] for their particle laden two-phase flows. In this work, we consider the gaseous flow field and neglect the particle calculation. Despite the absence of particle distribution here we study the effects of swirl on the unsteady flow dynamics, mean quantities, turbulence fluctuations and passive scalar distribution while validating the LES results with available experimental data.

In the following section we describe the governing equations. Section 3 discusses the numerical details including numerical discretisation, geometry and boundary conditions and simulation details. The main part of the paper (section 4) discusses the results obtained from LES calculations and finally the conclusions will close the paper.

2. GOVERNING EQUATIONS

The LES technique is based on the explicit simulation of the larger scales whilst the effect of the smaller scales (the so called sub-grid scales) are modelled using a sub-grid scale (SGS) model. The governing equations are the spatially filtered incompressible mass, momentum and passive scalar equations and can be written as:

$$\frac{\partial \overline{u}_j}{\partial x_j} = 0\,, \tag{1}$$

$$\frac{\partial \overline{u}_i}{\partial t} + \frac{\partial (\overline{u}_i \overline{u}_j)}{\partial x_j} = -\frac{1}{\rho}\frac{\partial \overline{P}}{\partial x_i} + \frac{\partial (2\nu \overline{S}_{ij})}{\partial x_j} - \frac{\partial (\tau_{ij})}{\partial x_j}\,, \tag{2}$$

$$\frac{\partial \overline{c}}{\partial t} + \frac{\partial (\overline{u}_j \overline{c})}{\partial x_j} = (\frac{\nu}{\sigma})\frac{\partial^2 \overline{c}}{\partial x_j \partial x_j} - \frac{\partial \gamma}{\partial x_j}\,, \tag{3}$$

where $u_i, \rho, p, \nu, c, \sigma$ denote the velocity, density, pressure, kinematic viscosity, passive scalar concentration, and laminar Schmidt numbers, and the strain rate tensor, $S_{ij} = \frac{1}{2}\left(\frac{\partial \overline{u}_i}{\partial x_j} + \frac{\partial \overline{u}_j}{\partial x_i}\right)$. Here $\sigma = 0.7$.

The terms $\tau_{ij} = \left(\overline{u_i u_j} - \overline{u}_i \overline{u}_j\right)$ in equation (2) and $\gamma = (\overline{u_j c} - \overline{u}_j \overline{c})$ appearing in equation (3) result from the unresolved sub-grid scale contributions and hence subsequent modelling is required to close the filtered momentum equations and filtered scalar equation. Present work used the Smagorinsky [27] eddy viscosity model to calculate the SGS stress tensor $\tau_{ij} = \left(\overline{u_i u_j} - \overline{u}_i \overline{u}_j\right)$ such that

$$\tau_{ij} - \frac{1}{3}\delta_{ij}\tau_{kk} = -2\nu_{sgs}\overline{S}_{ij} \tag{4}$$

and the SGS scalar flux $\gamma = (\overline{u_j c} - \bar{u}_j \bar{c})$ such that

$$\gamma = \frac{-\nu_{sgs}}{\sigma_t} \frac{\partial \bar{c}}{\partial x_j} \tag{5}$$

The eddy viscosity ν_{sgs} is given as a function of the filter size and strain rate

$$\nu_{sgs} = C_s \bar{\Delta}^2 \left| \bar{S} \right| \tag{6}$$

where C_s is a Smagorinsky [27] model parameter and $|\bar{S}| = (2\bar{S}_{ij}\bar{S}_{ij})^{\frac{1}{2}}$. This work used the localised dynamics procedure of Piomelli and Liu [28] to obtain the subgrid scale turbulent Schmidt number (σ_t) and the model parameter C_s appearing in equations (5) and (6).

3. NUMERICAL METHOD

A. Numerical discretisation

The mathematical formulations for mass, momentum and passive scalar are numerically solved by means of a pressure based finite volume method using the large eddy simulation code PUFFIN developed by Kirkpatrick et al. [29][30]. The code has been recently parallelised by Kirkpatrick [31] and the results presented in this paper have been obtained using the parallel version. Spatial discretisation is achieved using a non-uniform Cartesian grid with staggered cell arrangement. Second order central differences (CDS) are used for the spatial discretisation of all terms in both the momentum equation and the pressure correction equation. This minimises the projection error and ensures convergence in conjunction with an iterative solver. The diffusion terms of the passive scalar transport equation are also discretised using the second order CDS. The convection term of the passive scalar transport equation is

discretised using a third order QUICK with ULTRA flux limiter [32] to ensure that the solution remains monotonic.

The momentum and scalar transport equations are integrated in time using a hybrid second order Adams-Bashforth/Adams-Moulton scheme. The pressure correction method of Van Kan [33] and Bell et al. [34] which involves solving an equation for pressure correction rather than the pressure is used for the present work. The solution to this equation is then used to project the approximate velocity field that results from the integration of the momentum equations onto a subset of divergence free velocity fields. The time step is varied to ensure that the maximum Courant number $C_o = \Delta t u_i / \Delta x_i$ remains approximately constant where Δx_i is the cell width, Δt is the time step and u_i is the velocity component in the x_i direction. The solution is advanced with time steps corresponding to a Courant number in the range of $C_o = 0.3$ to 0.5. A Gauss-Seidel solver is used to solve the system of algebraic equations resulting from the numerical discretisation of momentum and passive scalar transport equations. The BiCGStab method with a Zebra Gauss-Siedel preconditioner using successive over relaxation (SOR) and Chebyshev acceleration is used to solve the algebraic equations resulting from the discretisation of pressure correction equation.

B. Computational domain and boundary conditions

Fig.1 shows the schematic of the combustor used for this study. The combustor length from the dump plane to the exit plane is 1.5m with a diameter of 194mm. The central jet has a diameter D=32mm surrounded by small bluff body type wall with D=38mm. This is surrounded by an annular jet with diameter D=64mm. A solid wall covers the remaining region of the inlet with D=194mm. The centre of the central jet is taken as the geometric centre line of the flow where $r = 0$ and $x = 0$. Here we employed a non-

uniform Cartesian grid and the extension of the computational domain in x,y and z directions are $194\times194\times1000mm$. The computational domain resolved with $100\times100\times140\approx1.4$ million grid points. The grid employed a uniform mesh with $64\times64\times75$ points in the centre region of the domain ($64\times64\times300mm$) which covers the flow region of interest including two inlet sections, shear layers and the centre recirculation region. The grid then expands for x and y directions with an expansion ratio of $\gamma_{xy}=\Delta x(i)/\Delta x(i-1)=1.07$ and an expansion ratio of $\gamma_z=1.08$ for z-direction. Therefore in the fine region, the ratio between the smallest resolved scale (filter width=$\overline{\Delta}$) and integral length scale ($l\approx D_{jet}$) is $\overline{\Delta}/l=(\Delta x\Delta y\Delta z)^{1/3}/D_{jet}\approx0.125$. Although we employed a Cartesian grid, the centre jet, annular jet, surrounding solid rings existing at the inlet and the combustor wall are blocked out to produce a cylindrical geometry similar to the experimental configuration.

The swirl number is defined as the ratio between the axial flux of the swirl momentum, G_ϕ ($\mathrm{kgm^2s^{-2}}$), to the axial flux of the axial momentum G_x ($\mathrm{kgm^2s^{-2}}$) multiplied by a characteristic length R (m). Here we take the radius of the swirl annulus as the characteristic radius. The swirl number is given by:

$$S=\frac{G_\phi}{RG_x}=\frac{\int_0^R UWr^2dr}{R\int_0^R U^2rdr} \tag{7}$$

where U (m/s) and W (m/s) are the mean axial and tangential velocities of the annular jet respectively. Here we discuss three test cases for three different tangential

inlet velocities for the annular inlet with fixed bulk axial velocities for the central and annular jets.

Case	Bulk axial velocity of the central jet (m/s)	Bulk axial velocity of the annular jet (m/s)	Bulk tangential velocity of the annular jet (m/s)
I	12.5	18.0	13.0
II	12.5	18.0	19.5
III	12.5	18.0	26.0

Table 1. Inflow boundary conditions. In case I, the bulk tangential velocity is 13 m/s corresponds to the swirl number of 0.47.

The inflow axial velocity for the central and annular jets and the inflow swirl velocity for the annular jet were specified using the power low velocity profile such that

$$< U >= C_0 U_j \left(1 - \frac{|y|}{r}\right)^{1/7} \tag{8}$$

where U_j is the bulk velocity, y the radial distance from the jet centre line and r the radius of the jet. We have used the constant $C_0 = 1.1$ to assign a correct mass flow rate as used by the experimental group [25][26]. The turbulence fluctuations are generated from a Gaussian random number generator and added to the mean velocity profiles. No-slip boundary conditions are used at the solid walls and a zero normal gradient boundary condition is used at the outflow. For the passive scalar, a top hat profile is used at the inlet such that the passive scalar value is 1.0 at central jet 0 elsewhere and a zero normal gradient condition is used at the outlet.

C. Parallel simulation details

In order to make LES an acceptable practical design tool with more efficient turnaround time, efficient solvers with parallel computing systems and large computational resources must be employed. Here a domain decomposition technique is employed in which the domain is divided into separate boxes. Each box is the same size, so the total number of cells must be divisible by the number of processes that the job will be distributed to. To make the LES algorithm portable, the standardised Message-Passing Interface (MPI) protocol is used for parallel communication. All three simulations were carried out for a long time period before beginning the data collection for statistical calculations. The simulations are carried out for the total time of 1.2s, which is approximately eight flow passes transiently (0.8s) and four flow passes for statistical calculations (0.4s) with the time step $\Delta t = 1.0e-5$. Each simulation used 20 processors and the corresponding wall clock times for case I, II and III are 13.5, 18.30 and 24.237 hours. We note that the total CPU time increases with increasing swirl number as a result of the Courant number condition on the maximum time step size.

5. RESULTS AND DISCUSSION

This section is divided into five subsections containing separate discussions. The first topic discusses the code validation, which is followed by sections describing the analysis of velocity field, coherent structures and vortex breakdown bubbles. The last section addresses the details of passive scalar mixing and its variation with swirl number for the three cases.

5.1 Code validation

For validation of the LES results, we have used the experimental data of Sommerfeld and Qiu [25][26] which is equivalent to case I in this work. Fig. 2 shows the detailed measured and computed radial profiles of the time averaged mean axial velocity at different positions along the axis. The comparison is shown at eight different axial locations ranging from x=3mm to x=315mm. A positive to negative change in the mean axial velocity indicates flow reversal and hence recirculation. Although a few discrepancies are apparent the LES results agree well with experimental data in both near and far field axial locations. The LES slightly overestimates the peak values above the annular region at x=25mm and slightly underestimates the centre region values velocity at x=85mm. The existence of the swirl velocity also eases the higher axial momentum generated by the inlet axial velocities and hence increases the spread rate of the axial velocity in the radial direction.

Comparison of the predicted and measured swirl velocity is shown in Fig. 3, and the agreement is excellent for most axial locations. The LES predictions slightly overestimate the peak values at x=25mm and 52mm but this is the only significant discrepancy seen for the mean swirling velocity. The calculations are able to predict the correct trend for the mean swirling velocity, which is generally challenging in numerical simulations. Since the swirl velocity component is introduced from the annular jet with swirl number 0.47, the radial profiles of the mean swirl velocity have higher values above the annular inlet.

Figs. 4 and 5 show comparisons of measured and computed root mean square (rms) fluctuations of axial and swirling velocities. The LES calculations predict the peak rms axial velocity values at most axial locations and capture sharp changes of the

axial velocity fluctuations particularly well. However, the calculations slightly underestimate the peak values at x=3mm and 52mm above the annular inlet. In addition, the LES results under predict the centreline region values at x=85mm, 112mm and 155mm. These differences may be attributed in part to the fact that only the resolved components of the fluctuations are presented for the LES results. The radial profiles of the rms axial fluctuations at downstream axial locations closely follow the radial shape of the mean axial velocity at far-field axial locations (x=155m, 195mm and 315mm). The agreement between the calculations and measurements for the rms swirl velocity (Fig. 5) is good at most axial locations. It can be observed that both the axial and swirl fluctuations values are very similar at downstream axial locations. The rms swirl fluctuations (Fig. 5) also follow the same profile shape as axial fluctuations in the far field (x=195mm, 315mm). The magnitude of the all three rms fluctuations and their distributions show significant anisotropy of turbulence inside the central recirculation and corner recirculation regions and the present LES computations predict the peak values as well as profile shapes. Given the complexity of the coannular swirling flow field, LES results are particularly useful for identifying sharp changes in regions where we can expect intermittent turbulent behaviour. The turbulence values are generally high along the boundary of the VB bubble while mean velocities are quite low inside the vortex bubble and the present calculation confirms this finding for the simulated coannular swirl jet.

5.2 Analysis of the velocity field

Figs. 6 (a-c) and 7 (a-c) show snapshots of the filtered axial and swirling velocities for cases I, II and III. As seen in Figs 6(a-c) close to the inlet the axial velocity shifts radially with increased swirl velocity as a result of increased centrifugal force. The

centreline velocity decays more rapidly with increasing swirl number and hence the central recirculation zone moves towards the inlet. In order to demonstrate the effect of swirl strength, Figs. 7(a-c) show the snapshots of the filtered swirl velocity with increasing swirl number. Again, the structure of the swirling jets changes with increasing swirl number. The inlet swirl velocities for case I, II and III are 13.0 m/s, 19.5 m/s and 26.0 m/s respectively. As the swirl number increases, the momentum of the annular jet moves more rapidly away from the centreline demonstrating that the jet spreads more rapidly with increasing swirl number.

Figs. 8(a-c) show instantaneous velocity vectors for case I, II and III respectively. These plots indicate the increasing complexity of the flow with increased swirl number. The velocity vector field for the case I is noticeably different from case II and III. However, similarities can be seen in the velocity fields for case II and III. In Fig. 8(a), the vector field shows a relatively smooth decay and only starts to perturb significantly in the intermediate region. At higher swirl velocities the swirl causes rapid axial momentum decay and also creates more rotational vortices in the near field region. These rotational vortices interact with the swirl velocities to make complex flow patterns as seen in both Figs. 8 (b) and (c). The velocity vector fields also show different vorticity structures in the central and corner recirculation zones which indicate a high level of turbulence in the regions where we expect precession behaviour.

5.3 Analysis of the coherent structures

Figs. 9 (a-c) show the coherent structures known as Precessing Vortex Cores (PVC) associated with local minima of the pressure field. Although the pressure fluctuation

is more suitable to demonstrate PVC structures [35], here we used instantaneous pressure. Despite slight differences appearing in the PVC structures, helical type vortices are observed for all three cases. The plots also reveal that an increased swirl number widens the angle of the PVC structure with respect to the central axis. Garcia et al. [36] found that more than one structure can appear at certain instants in time in a PVC such that one forms in the inner region of the jet and another forms in the outer region. However, most of the time a single vortex is dominant as appears in Figs. 9(a-c). More investigations on PVC structures appearing in confined coannular combustors is needed and is now timely, as key problems associated with combustion instabilities in lean burn gas turbine systems are directly linked with PVC structures and their dynamical behaviour in the near field region (primary zone of the combustor).

Figs. 10-12 show the power spectra for case I, case II and case III respectively. The power spectrum is constructed by applying the Fast Fourier Transform (FFT) to the instantaneous axial velocity. The selected spatial location is situated at x=30mm (axial location) and r=25mm in the region where precession motion can be expected. A pair of points is used in either side of the centre jet. The power spectrum in Fig. 10 for the case I (S=0.47) shows many peaks at different frequency levels and therefore cannot identify a distinct precession frequency for a cyclic motion. Fig.11. shows a distinct precession frequency for case 2 (S=0.7) at approximately 300Hz and thus forms more stable precession than that appears for case 1. As seen in Fig. 12, the power spectrum for case 3 with high swirl number (S=0.94) shows a distinct precession around 200Hz and therefore the precession motion appears to be periodic than the other two cases. Therefore the power spectra indicates that the low frequency

distinct peaks for high swirl number and the highest peak value shift more towards low frequency level with increased swirl number. The power spectra further confirms the relation between swirl number and low frequency oscillation for a coannular swirl combustor and gives some evidence to handle the critical swirl number for a stable flame in the presence of combustion. The existing theoretical correlations can be used to further clarify the issues identified in this power spectra analysis.

Since we observed the distinct precession frequencies for high swirl number, we also produced the probability density functions (PDF) of the instantaneous axial velocity at similar spatial location. Fig. 13 shows the PDF of axial velocity for case I (a), case II (b) and case III (c) respectively. As seen in Fig. 13 the PDF shapes follows a Gaussian distribution for low swirl number and then shifting to a Non-Gaussian shape with an increased swirl number. A further increase of the swirl should arguably create a Non-Gaussian PDF distribution and might convert to delta function with certain level of high swirl. Therefore, the strength of swirl exhibits a couple phenomena between precession frequency and non-Gaussian PDF distributions. However, further investigation is required to confirm the couple relation between critical swirl number, distinct precession frequencies and Non-Gaussian PDF distributions, which will certainly help us to improve the mixing patterns of a confined coannular swirl combustor.

5.4 Analysis of the vortex breakdown bubbles (VBB)

Figs. 14(a-c) show the contour plot of mean axial velocity obtained from the time average mean axial velocity for case I, II and III respectively. Here, dashed lines indicate negative contour lines and the solid line indicates the contour line for the zero

mean axial velocity which has been used to identify the extent of the VB bubble position in the axial and radial directions. As seen in Fig. 10(a) a central recirculation zone known as the vortex breakdown bubble (VBB) forms in the central region and the zero contour line starts at approximately 50mm axially from the inlet plane. Figs. 10 (b) and (c) indicate that the zero contour line of the VB bubble shifts towards the inlet plane with increased swirl number. This happens due to the increase in swirl momentum and thus increases in centrifugal force which effectively increases the adverse pressure gradient. The increase in swirl also reduces the axial velocity on the centreline and hence more separate layers can be formed. The zero contour lines start at axial distances of approximately 20mm and 5mm for case II and III respectively.

In addition, the swirl has a lesser effect on the radial extent of the VBB compared with the axial extent. In fact the radial extent is largely unchanged with respect to swirl number. This might be attributed to the presence of the combustor wall which prevents further radial expansion of the VB bubble. Both the rms axial and swirling velocity fluctuation values are high on the boundary of the VB bubble and hence we can expect rapid changes of the velocity fluctuations in this surrounding area which may be attributed to small scale intermittency. Hence further investigations on variation of the turbulence structures around the VB bubbles with respect to increased swirl number may useful to detect small scale intermittency for swirl based applications.

Figs. 15-16 show the effect of swirl on axial and swirl velocity at x/D=2 and x/D=6. Here D is the diameter of the annular jet, u_m and u_{mo} is the mass axial and initial mass axial velocities, w_m and w_{mo} is the mass swirl and initial mass swirling velocities

respectively. Fig. 15 shows that the axial and swirl velocities at x/D=2 decay more rapidly with high swirl number when compared with their initial maximum values. As seen in Fig.16 at far downstream (x/D=6), the axial velocity decays more rapidly with high swirl number while decays of the swirl velocity has less effect for high swirl. These plots further clarify the swirl effect on radial and axial pressure gradients. Fig.17 shows the progressive axial extent of the centre recirculation zone as a function of swirl number and the correlation between swirl number and axial extent of the centre recirculation zone is approximately linearly related.

5.5 Analysis of the passive scalar field

Figs. 18 (a-c) show the snapshots of filtered passive scalar fields for case I, II and III respectively. The snapshots show large variations with increased swirl number and demonstrate very large perturbations linked with the swirl number. The contour plots of the mean passive scalar (Figs. 19 (a-c)) further demonstrate the variation of passive scalar with respect to increased swirl number. As seen in Figs. 19 (a-c) the mean passive scalar distribution spreads more in the radial direction with increasing swirl number. Furthermore, the centreline passive scalar decays much faster with increased swirl number.

Figs. 20 and 21 show radial profiles of the time averaged mean passive scalar and its variance at different axial locations. The profiles were produced to cover the near field, intermediate region and far field axial locations. The plots contain three data sets such that the dashed-dot-dashed, dashed and solid lines indicate results for the case I, II and III respectively. As seen in Fig. 20, the radial profiles of time averaged mean passive scalar show the mixing pattern for different swirl strengths at six axial

locations. Despite the differences of the peak values, the profiles of the mean passive scalar are quite similar at the first two axial locations (x=10mm, 40mm). Further downstream, the passive scalar is seen to mix much more rapidly in the higher swirl cases, due to the increased intensity of both the swirl and the VB bubble. Fig. 21 shows radial profiles of the passive scalar variance at six different axial locations. The plots of the passive scalar variance show high peaks in the near field for the highest swirl case due to the existence of high turbulence structures along the boundary of the breakdown bubble. However, further downstream the radial spread of the passive scalar variance is similar for all three cases and the highest swirl case has the smallest centreline variance value which is close to zero at downstream locations (x=100mm, 120mm, 150mm).

An efficient mixing is critical to achieve clean combustion in reacting flows systems, whether they are powered by gaseous or liquid fuels. The effect of swirl on mean passive scalar distributions and its variance in non-reacting flows can be used to consider the possible heat release structures for active scalars in a coannular swirl combustor. Heat release occurs from chemical reactions and acts as a major driving force for unsteady flow oscillations in combustion systems. Therefore the combination of swirl and heat release further increase the complexity and thus need careful consideration for the critical swirl number, heat release factor and pressure oscillations as the combination of these parameters should produce combustion instabilities. Since the combustion phenomena in LES acts in the small scales the energy transfer from large scale to small scale along with heat release can be critically affected by the swirl number. In such situations, the flame is anchored by the centre recirculating flow and an existence of the precession motion as observed in this

investigation might cause flame flashback, thus driving the flame upstream toward the inlet of the combustor especially for lean premixed combustion. An effort is currently underway to fully investigate the effect of swirl on combustion dynamics in confined and unconfined situations and results will be reported in the near future.

6. CONCLUSIONS

The primary focus of this work was to examine the effects of swirl on the flow field and mixing in a confined coannular swirl combustor using Large Eddy Simulation (LES). The combustor model here was a particle laden swirl combustor experimentally investigated by Sommerfeld and Qiu [25][26]. Here we used both instantaneous and time-averaged data to describe the structure and topology of flow fields and mixing in swirl stabilised coannular combustor. We found that an increasing swirl number leads to an increase in the rate of decay of axial momentum due to both viscous and inviscid effects. The simulations also generated PVC structures for all three cases and an increased swirl velocity was seen to shift the VB bubble towards the inlet. The power spectra indicate the development of periodic precession motion with high swirl strength and the probability density functions demonstrate the shifting behaviour of Gaussian to non-Gaussian distributions with increased swirl number. An increase in the passive scalar mixing is also observed at higher swirl numbers and the scalar variance is seen to contain high peaks in the region of the VB boundaries. Since we observed highly anisotropic turbulence regions in the near field, identification of instability mechanisms associated with precession motion in this swirl combustor would help to explore more details of combustion flashback of gas turbine type combustors especially for lean burn combustion situations.

REFERENCES

[1] Lieuwen, T Yang, V. Combustion Instabilities in gas turbine engines: operational experience, fundamental mechanisms, and modelling, Progress in Astronautics and Aeronautics, AIAA publisher, 2005

[2] Syred N. A review of oscillation mechanisms and the role of the precessing vortex core (PVC) in swirl combustion systems. Prog. Energy. Combust. Sci 2006; 32: 93-161

[3] Squire, H.B. Analysis of the vortex breakdown phenomena, Academic verlag, 306, 1962

[4] Randall, J.D, Leibovich, S, The critical state: a trapped wave model of vortex breakdown, J. Fluid Mech., 53, 495-508, 1973

[5] Krisbus, A, Leibovich, S, Instability of strong non-linear waves in vortex flows, J. Fluid Mech., 269, 247-265, 1994

[6] Chanaud RC. Observations of oscillatory motion in certain swirling flows. J. Fluid. Mech 1965; 21(1): 111-121

[7] Froud D, O'Doherty T, Syred N. Phase averaging of the precessing vortex core in a swirl burner under piloted and premixed combustion conditions. Combust. Flame 1995; 100: 407-417

[8] Pierce, C, Moin, P. Method for generating equilibrium swirling inflow conditions, AIAA J., 36, 1325-1327, 1998

[9] Kim, W, Menon. S, Mongia, H. Large eddy simulation of a gas turbine combustor flow, Combust. Sci. Tech. Vol. 143, 25-63, 1999

[10] Grinstein, F.F, Young, T.R, Gutmark, E.J, Li, G.Q,Hsiao, G, Mongia, H.C. Flow dynamics in a swirl combustor', J. Turb Vol. 3, paper 30, 2002

[11] Apte, S.V, Mahesh, K, Moin, P, Oefelein, J.C.Large eddy simulation of swirling particle laden flows in a coaxial jet combustor, Int J Multiphase Flows 29(8), 1311-1331, 2003

[12] Lu, X, Wang, S, Sung, H, Hsieh, S, Yang, V. Large eddy simulations of turbulent swirling flows injected into a dump chamber, J Fluid Mech. 527, 171-195, 2005

[13] James, S, Zhu, J, Anand, M.S, Large eddy simulation of turbulent flames using filtered density function method, Proc. Combust. Inst. 31, 1737-1745, 2007

[14] Wenger B, Maltsev A, Schneider C, Sadiki A, Dreizler A, Janicka J. Assessment of unsteady RANS in predicting swirl flow instability based on LES and experiments, Int. J. Heat Fluid Flow 25, 28-36, 2004

[15] Wang S, Yang V, Hsiao G, Hsieh S, Mongia H, Large eddy simulations of gas turbine swirl injector flow dynamics. J. Fluid. Mech 583, 99-122, 2007

[16] Pierce, C.D. and Moin, P.Progress variable approach for LES of non-premixed turbulent combustion, J. Fluid Mech. 504, 73-97, 2004

[17] Di Mare, Jones. W. Menzies. K. Large eddy simulation of a model gas turbine combustor, Combust. Flame 137(3), 278-294, 2004

[18] Mahesh, K, Constantinescu, G, Apte, S, Iaccarineo, G, Ham, F, Moin, P., 2006, Large eddy simulation of turbulent flow in complex geometries, ASME J. App. Mech. 73,. 374-381

[19] Bioleau, M, Staffelbach, G, Cuenot, B, Poinsot, T, Berat, C. LES of an ignition sequence in gas turbine engine, Combust. Flame, 154, 2-22, 2008

[20] Boudier, G, L.Y.M. Gicquel, T.J. Poinsot. Effects of mesh resolution on large eddy simulations of reacting flows in complex geometry combustors, Combust. Flame, 155, 196-214, 2008

[21] Roux, A, Gicquel, L.Y.M, Sommerer, Y, Poinsot, T.J, 2008, Large eddy simulation of mean and oscillating flow in a side dump ramjet combustor, Combust Flame 152, 154-176

[22] Sankaran, V, Menon, S. LES of spray combustion in swirling flows, J. Turbulence 3, 11-23, 2002

[23] Reveillon, J, Vervisch, L., 2000, Spray vaporization in nonpremixed turbulent combustion modelling: a single droplet model, Combust Flame 121, 75-90

[24] Patel, N, Menon, S. Simulation of spray-turbulence-flame interactions in a lean direct injection combustor, Combust. Flame, 153, 228-257, 2008

[25] Sommerfeld M, Qiu, H.H. Detailed measurements in a swirling particulate two-phase flow by a phase-Doppler anemometer, Int. Journal of Heat and Fluid Flow 1991; 12 (1), 20-28: 1991;

[26] Sommerfeld, M, Qiu, H.H. Characterisation of particle-laden confined swirling flows by phase-doppler anemometry and numerical calculation, Int. J. Multiphase flow 1993; 19 (6):1093-1127, 1993

[27] Smagorinsky, J. General circulation experiments with the primitive equations", M. Weather Review 1963; 91: 99-164

[28] Piomelli, U. and Liu, J. Large eddy simulation of channel flows using a localized dynamic model, Phy. Fluids 1995; 7: 839-848

[29] Kirkpatrick, M.P., Armfield, S.W. and Kent J.H. A representation of curved boundaries for the solution of the Navier-Stokes equations on a staggered three-dimensional Cartesian grid, J. of Comput. Phy. 2003; 184: 1-36.

[30] Kirkpatrick, M.P., Armfield, S.W., Masri, A.R. and Ibrahim, S.S. Large eddy simulation of a propagating turbulent premixed flame, Flow Turb. and Combust. 2003; 70 (1): 1-19.

[31] Kirkpatrick, M.P. and Armfield, S.W. On the stability and performance of the projection-3 method for the time integration of the Navier-Stokes equations, ANZIAM Journal, 2008: 49: C559 –C575.

[32] Leonard, B.P., Mokhtari, S. Beyond first order upwind: The ULTRA SHARP alternative for non-oscillatory steady-simulation of convection, Int. J. Num. Meth. Eng., 30, 729-766, 1990

[33] Van Kan, J. A second order accurate pressure correction scheme fir viscous incompressible flow., SIAM J. Sci. Stat. Comput. 7, 870-891, 1986

[34] Bell, J.B, Colella, P, Glaz, H.M. A second order projection method for the incompressible Navier-Stokes equations, J. Comput. Phys., 85, 257-283, 1989

[35] Frohlich, J, Mellen, C.P, Rodi, W, Tennerman, L, Leschziner, M.A. Highly resolved large eddy simulation of separated flow in a channel with streamwise periodic constrictions, J. Fluid Mech., 526, 19, 2005

[36] Garcia-Villalba, M, Frohlich, J, Rodi, W. Identification and analysis of coherent structures in the near field of a turbulent unconfined annular swirling jet using large eddy simulation, Physics of fluids, 18, 055103, 2006

FIGURE CAPTIONS

Fig. 1. Geometry of the configuration

Fig. 2. Comparison of mean axial velocity. Lines represent LES results, and symbols represent experimental measurements

Fig. 3. Comparison of mean swirling velocity. Lines represent LES results, and symbols represent experimental measurements

Fig. 4. Comparison of rms axial velocity. Lines represent LES results, and symbols represent experimental measurements

Fig. 5. Comparison of rms swirling velocity. Lines represent LES results, and symbols represent experimental measurements

Fig. 6. Snapshots of filtered axial velocity for case I (a), case II (b) and case III (c)

Fig. 7. Snapshots of filtered swirl velocity for case I (a), case II (b) and case III (c)

Fig. 8. Velocity vector fields for case I (a), case II (b) and case III (c)

Fig. 9. Precessing vortex cores (PVC) for case I (a), case II (b) and case III (c)

Fig. 10. Power spectrum at selected spatial locator for case 1

Fig. 11. Power spectrum at selected spatial locator for case 1

Fig. 12. Power spectrum at selected spatial locator for case 1

Fig. 13. Velocity probability density functions at selected spatial locator for case I (a), case II (b) and case III (c)

FIGURES

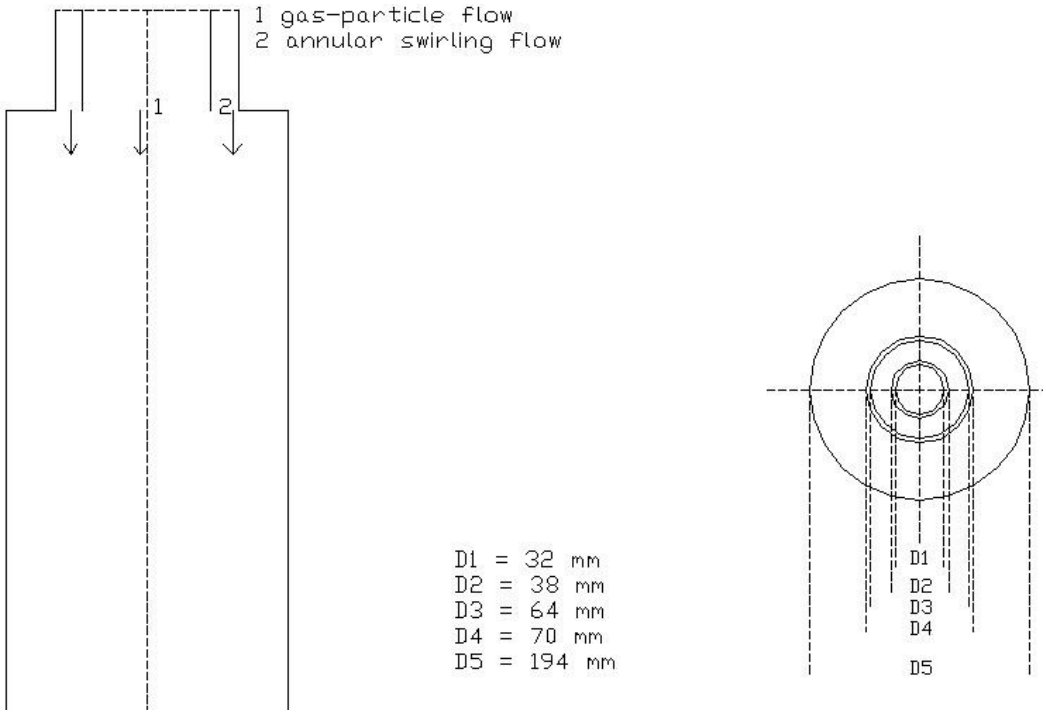

Fig. 1. Geometry of the configuration

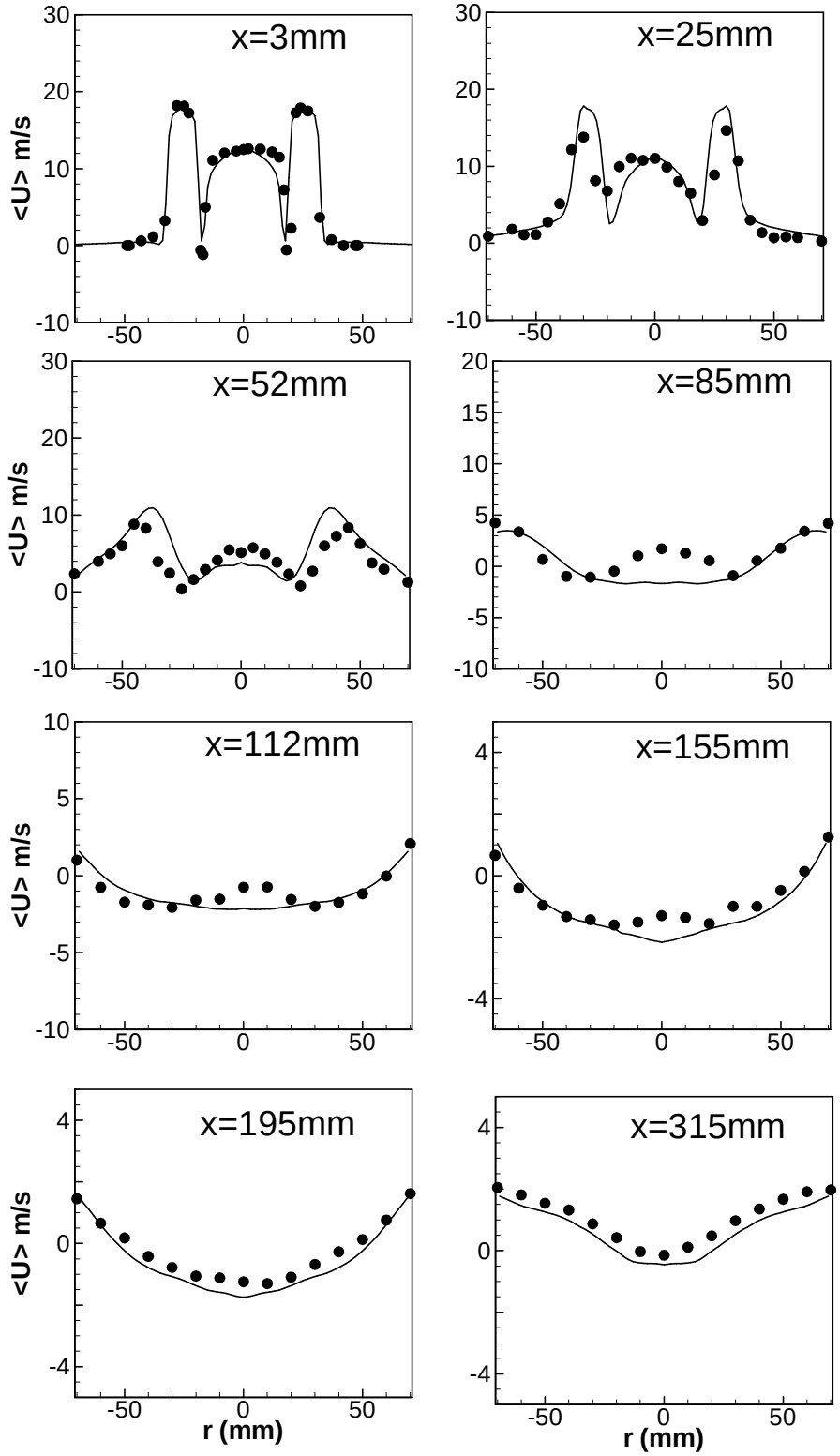

Fig. 2. Comparison of mean axial velocity. Lines represent LES results, and symbols represent experimental measurements

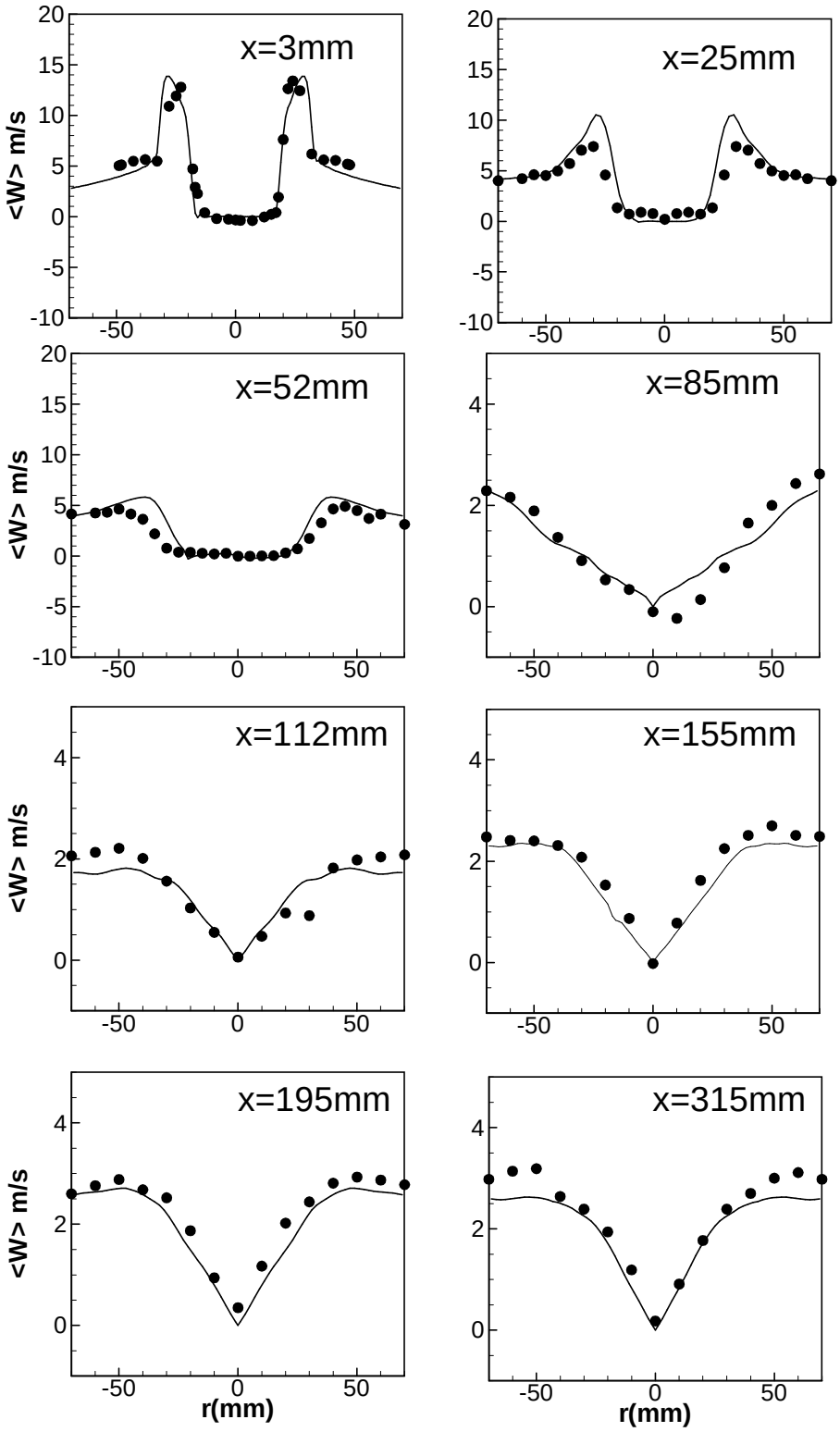

Fig. 3. Comparison of mean swirling velocity. Lines represent LES results, and symbols represent experimental measurements

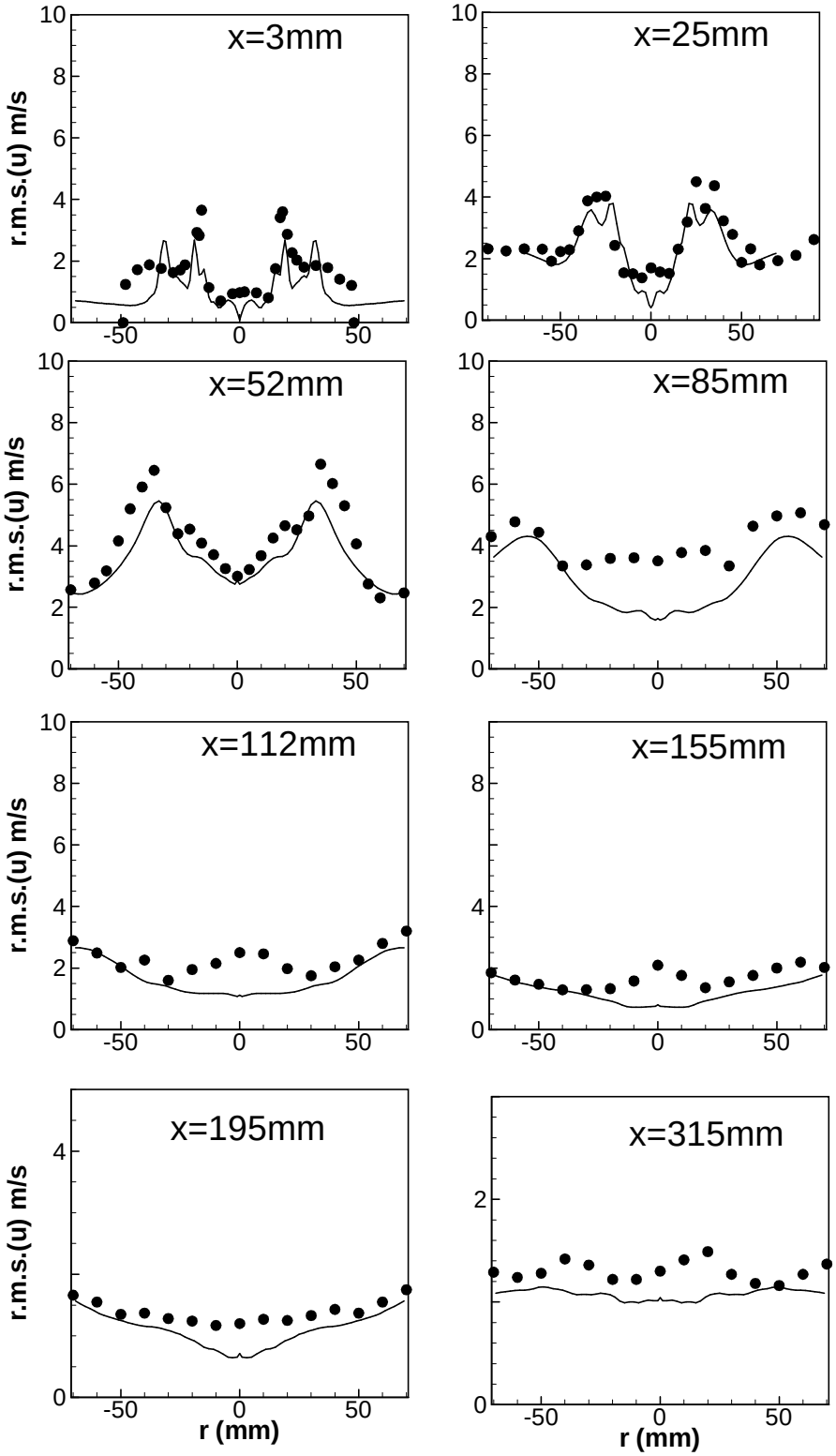

Fig. 4. Comparison of rms axial velocity. Lines represent LES results, and symbols represent experimental measurements

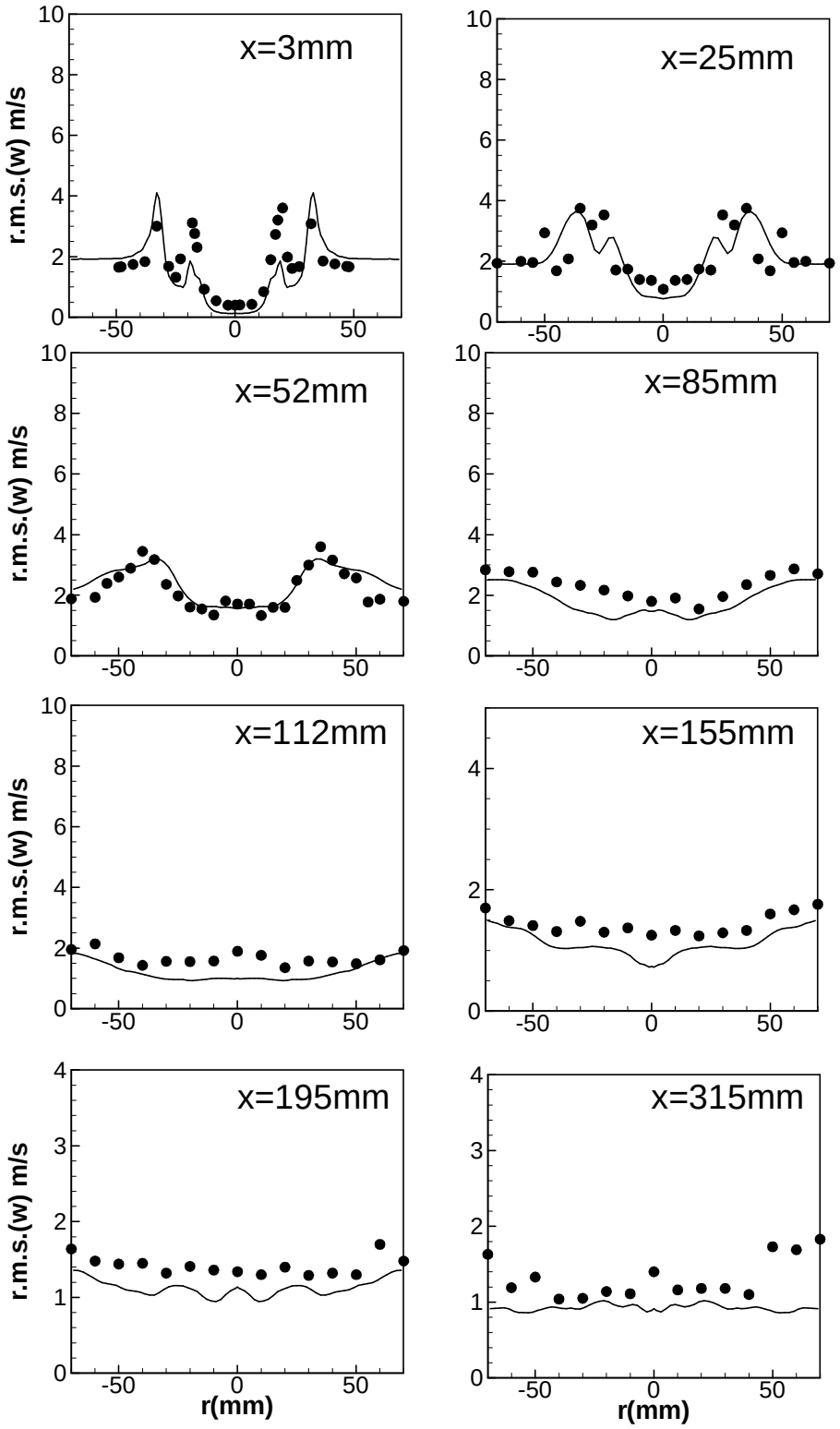

Fig. 5. Comparison of rms swirling velocity. Lines represent LES results, and symbols represent experimental measurements

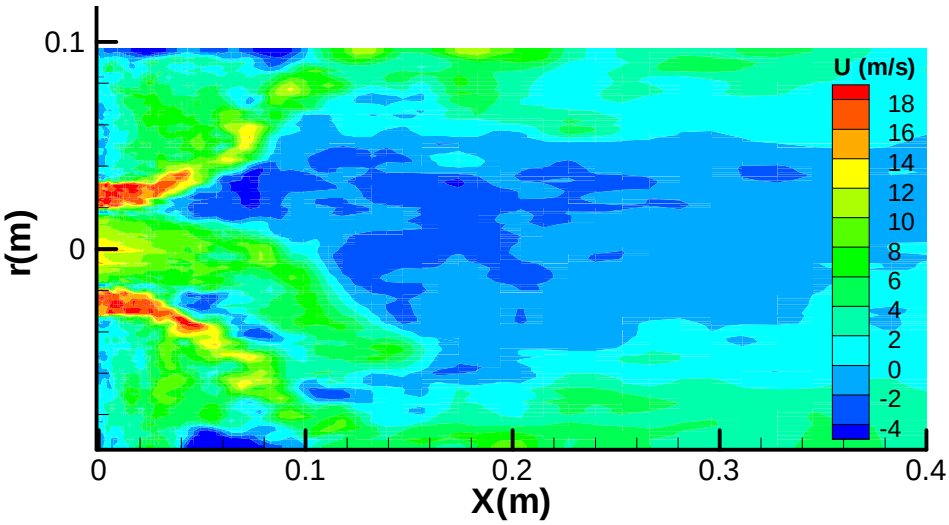

(a)

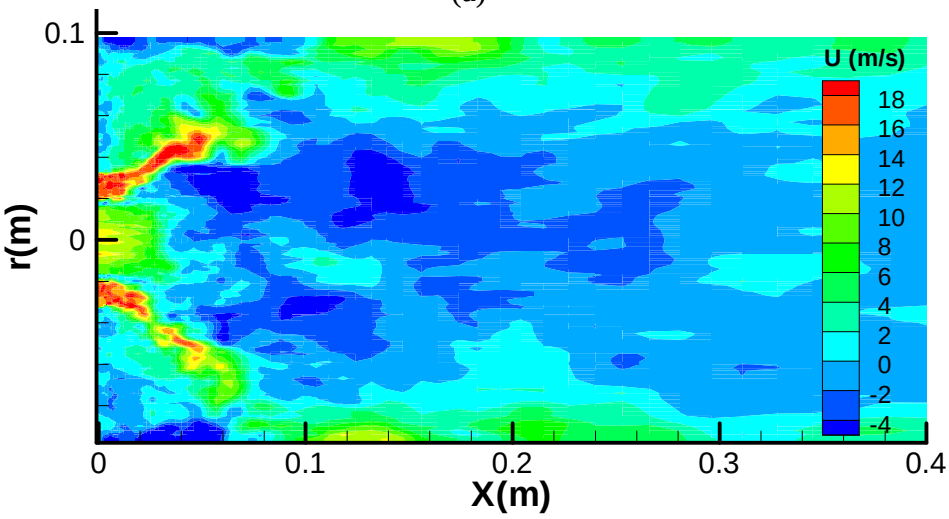

(b)

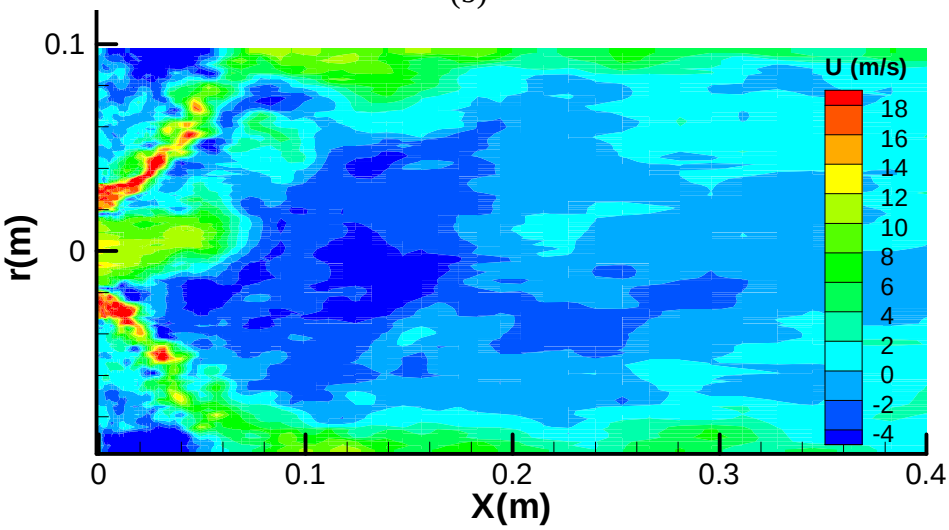

(c)

Fig. 6. Snapshots of filtered axial velocity for case I (a), case II (b) and case III (c)

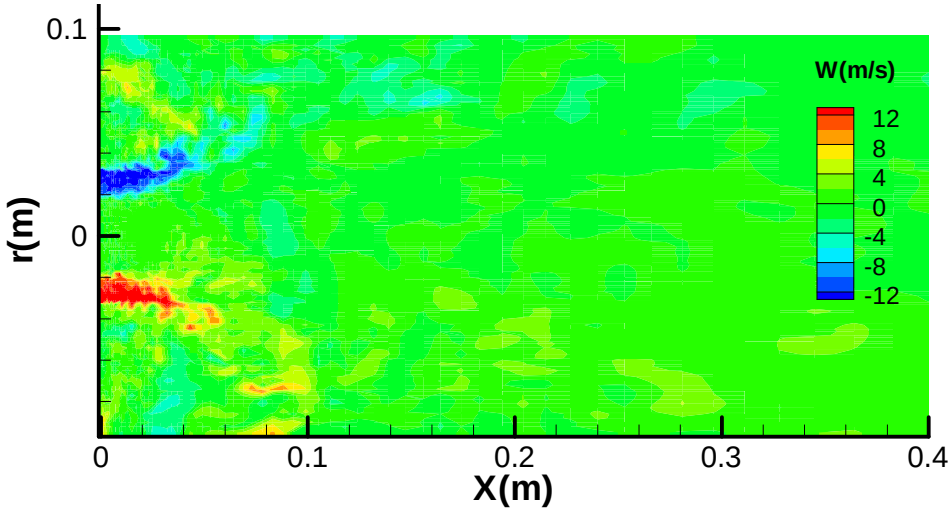

(a)

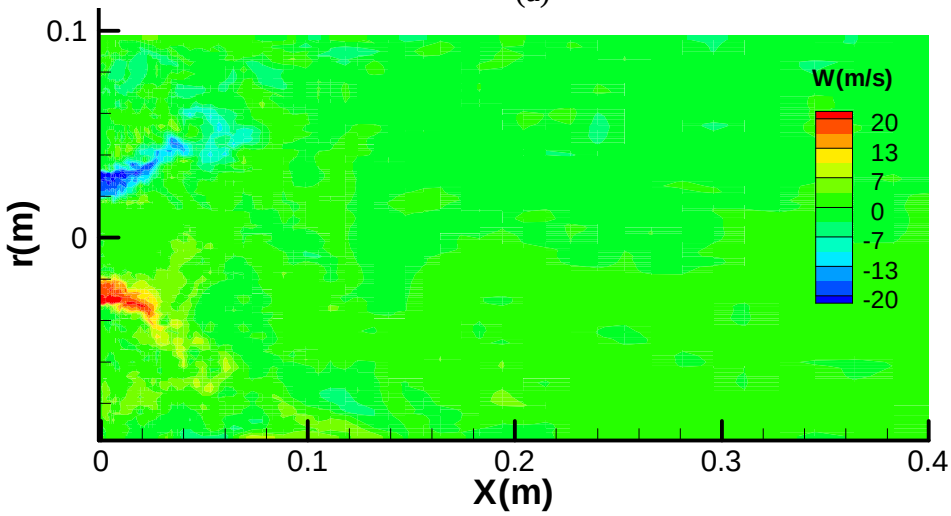

(b)

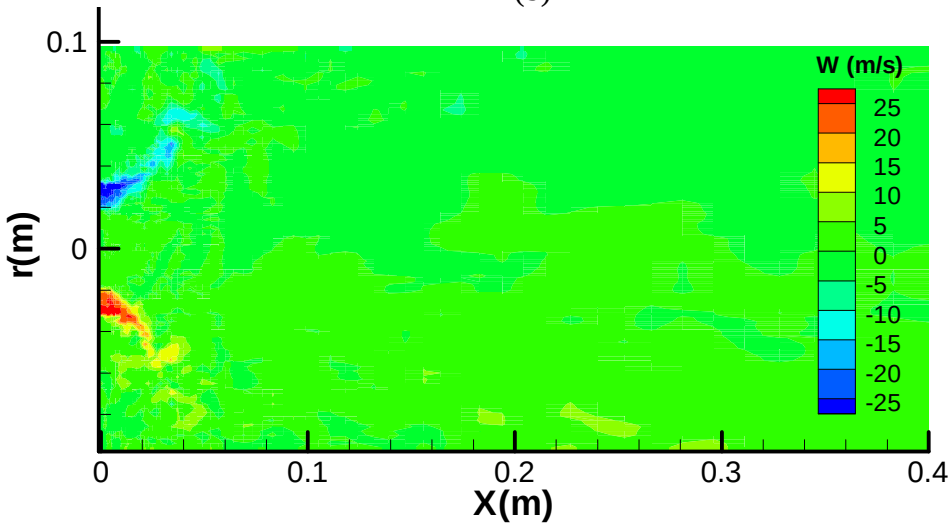

(c)

Fig. 7. Snapshots of filtered swirl velocity for case I (a), case II (b) and case III (c)

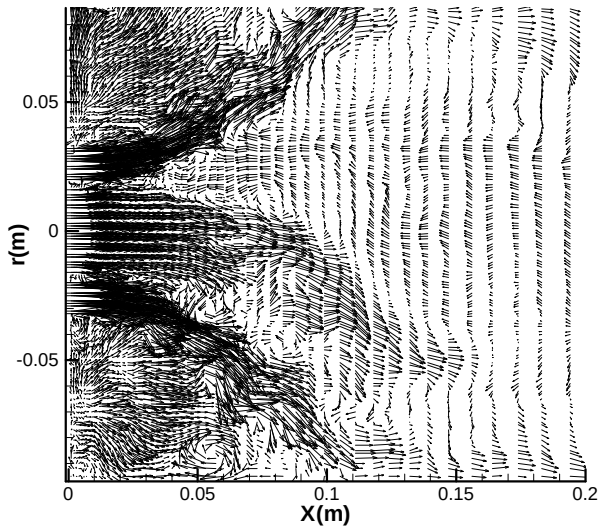

(a)

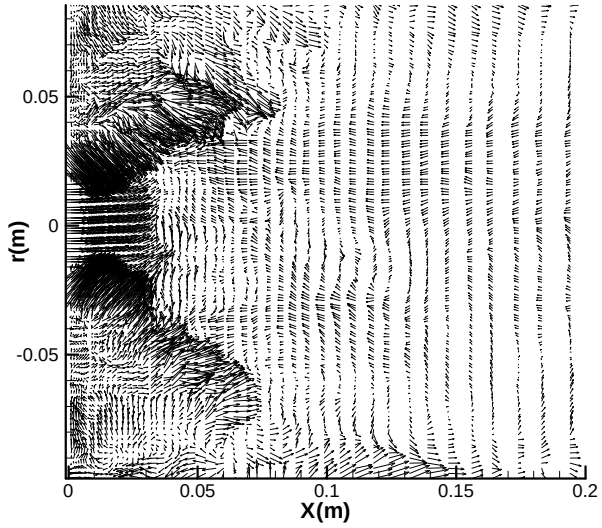

(b)

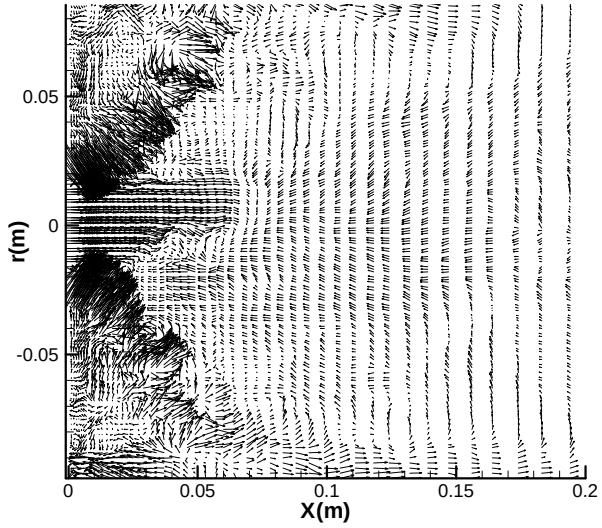

(c)

Fig. 8. Velocity vector fields for case I (a), case II (b) and case III (c)

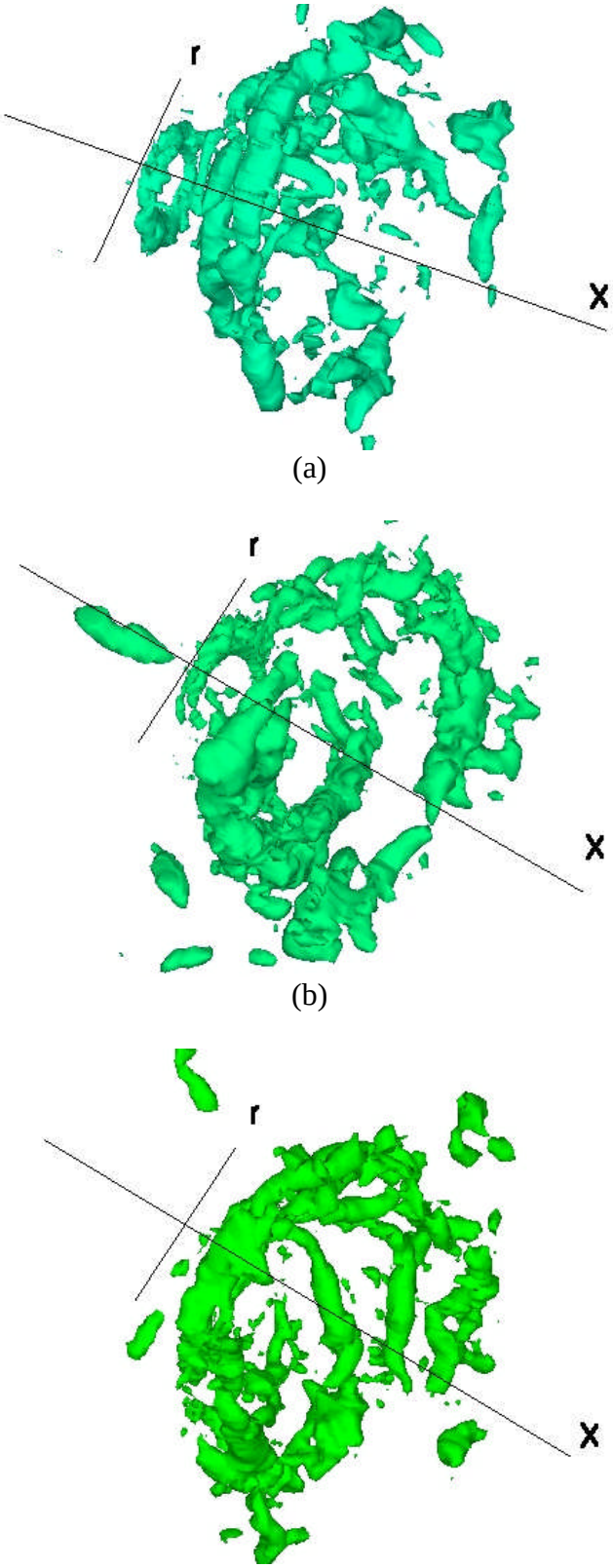

Fig. 9. Precessing vortex cores (PVC) for case I (a), case II (b) and case III (c)

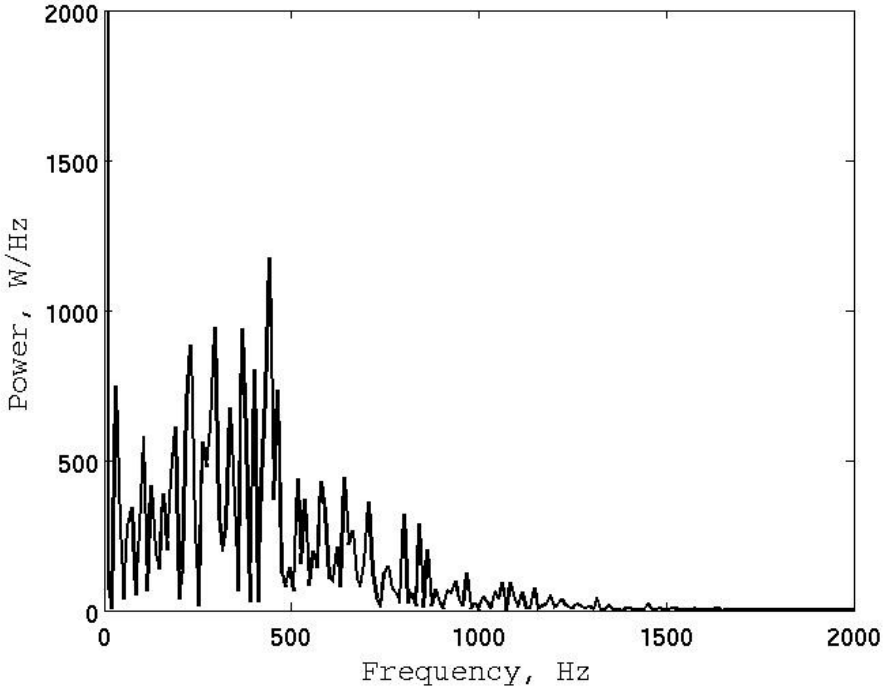

Fig. 10. Power spectrum at selected spatial locator for case 1

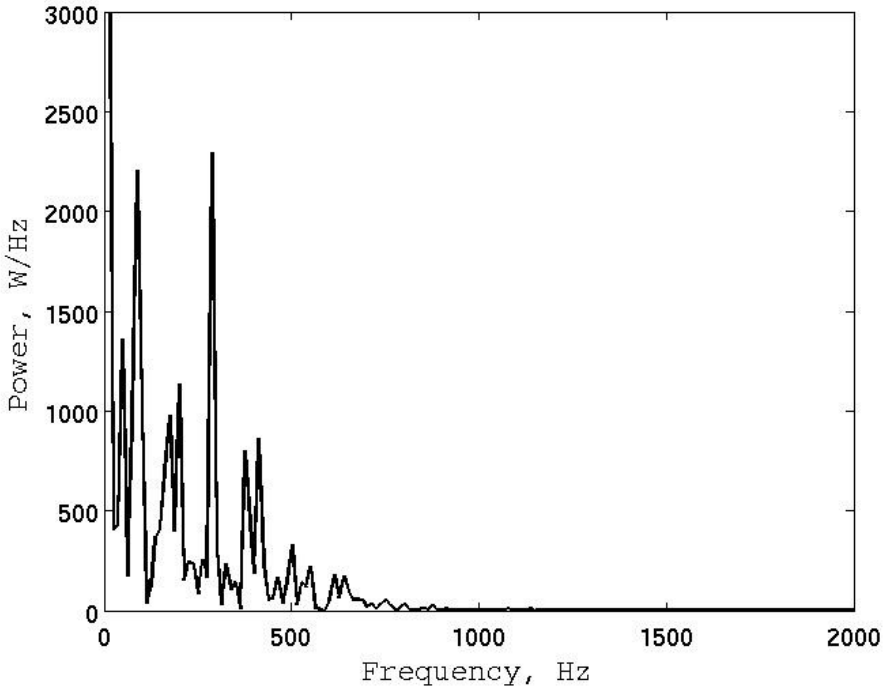

Fig. 11. Power spectrum at selected spatial locator for case 2

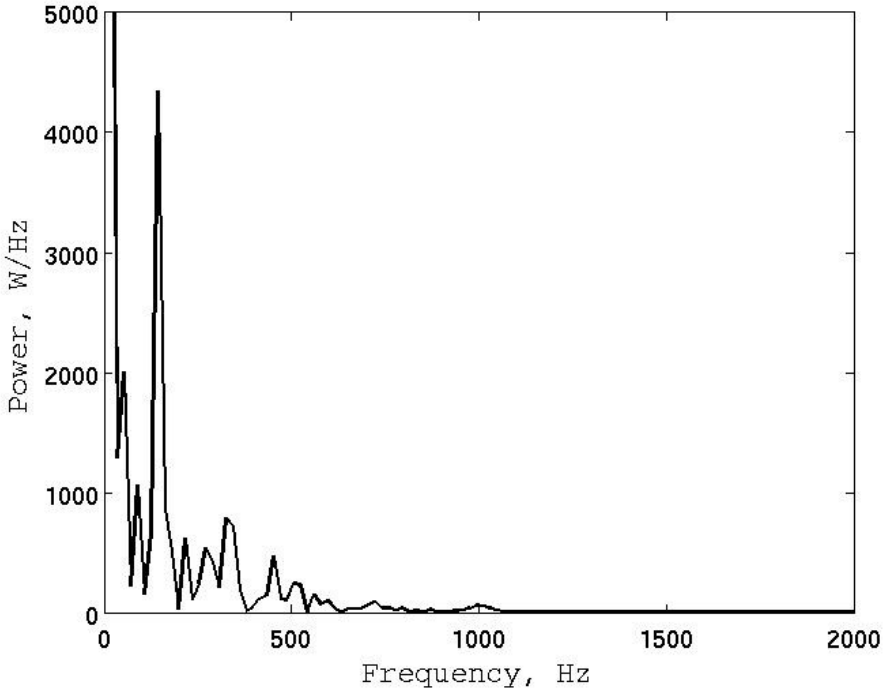

Fig. 12. Power spectrum at selected spatial locator for case 3

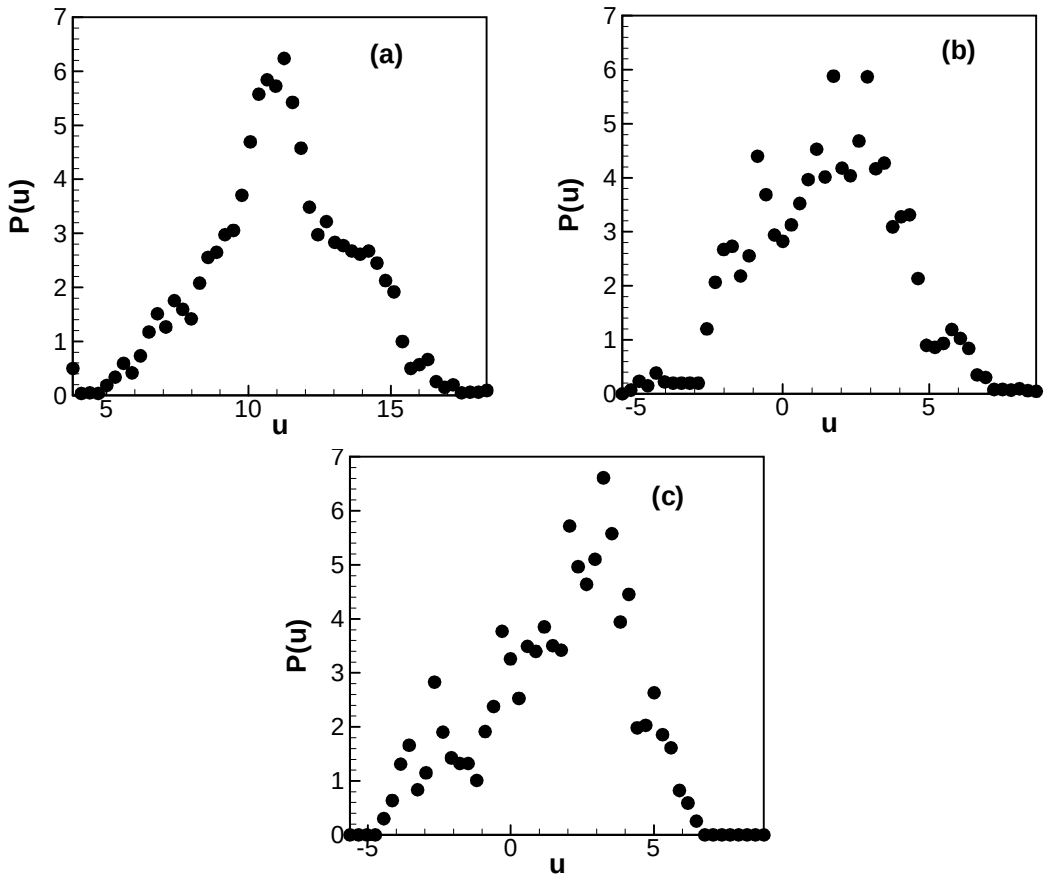

Fig. 13. Velocity probability density functions at selected spatial locator for case I (a), case II (b) and case III (c)

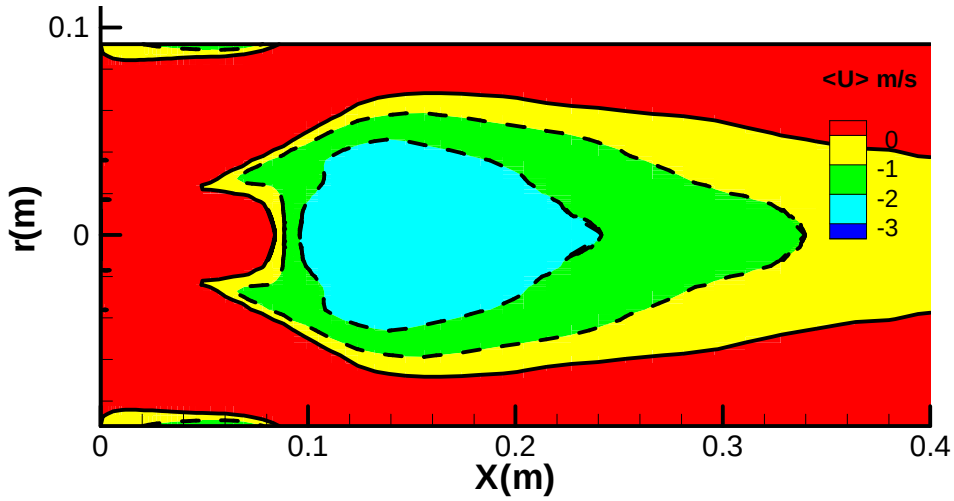

(a)

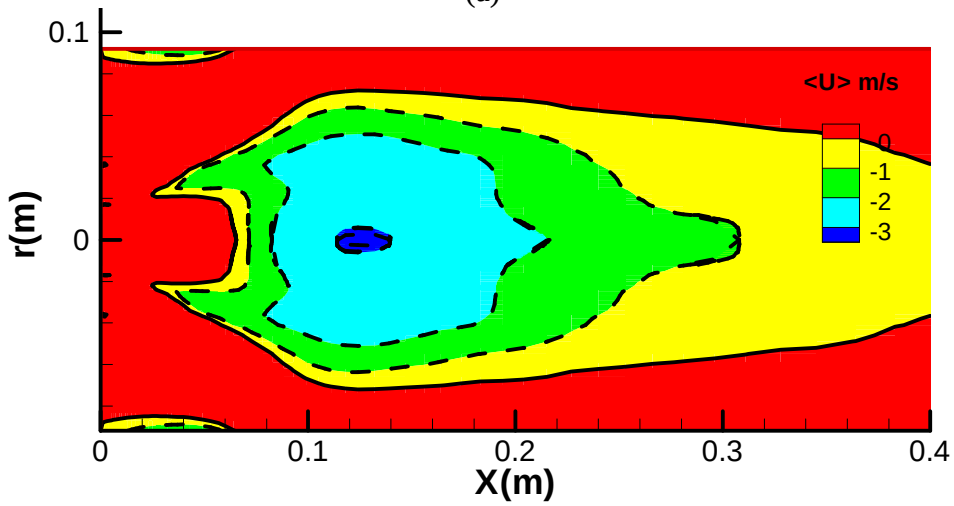

(b)

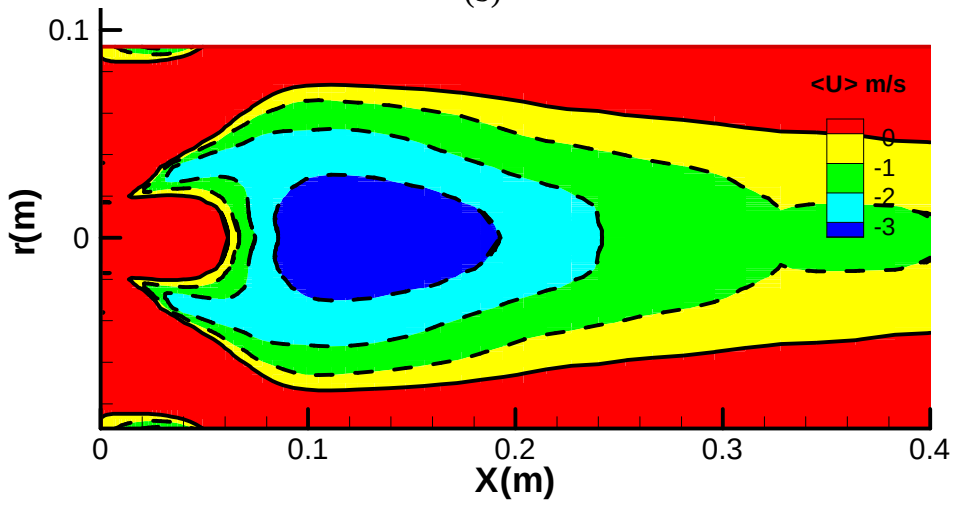

(c)

Fig. 14. Vortex breakdown (VB) bubbles for case I (a), case II (b) and case III (c)

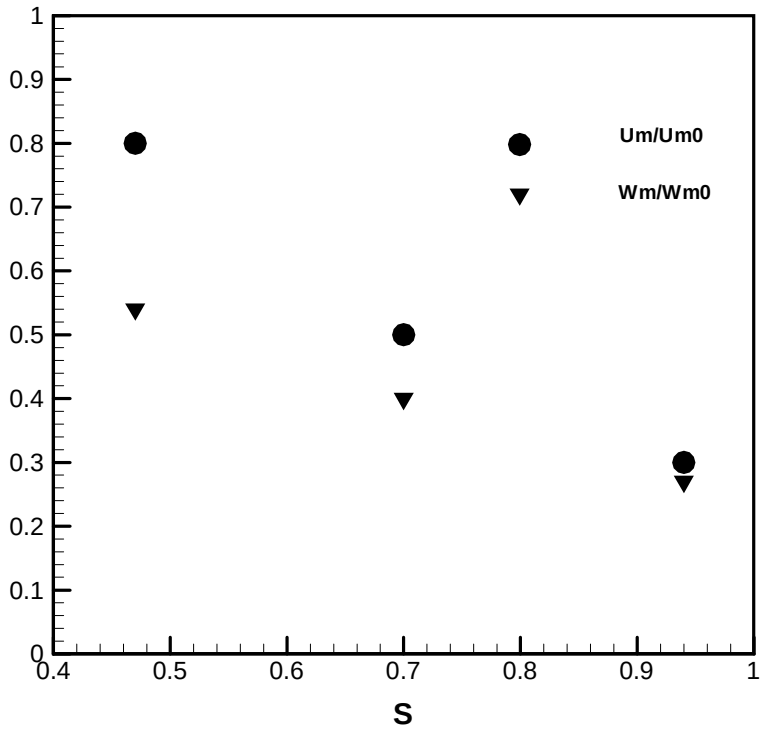

Fig. 15. Effect of S on axial and swirl velocity decay at x/D=2

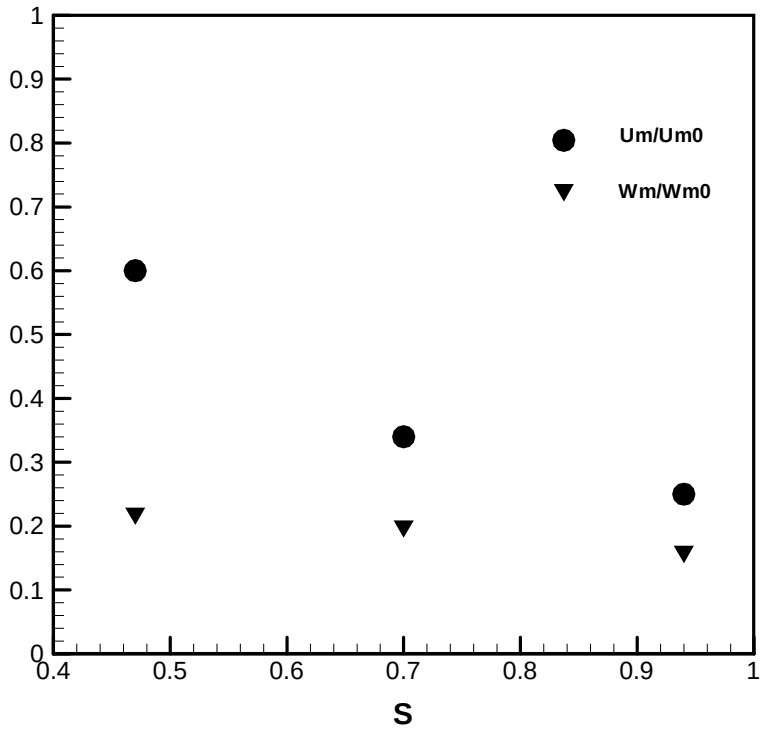

Fig. 16. Effect of S on axial and swirl velocity at x/D=6

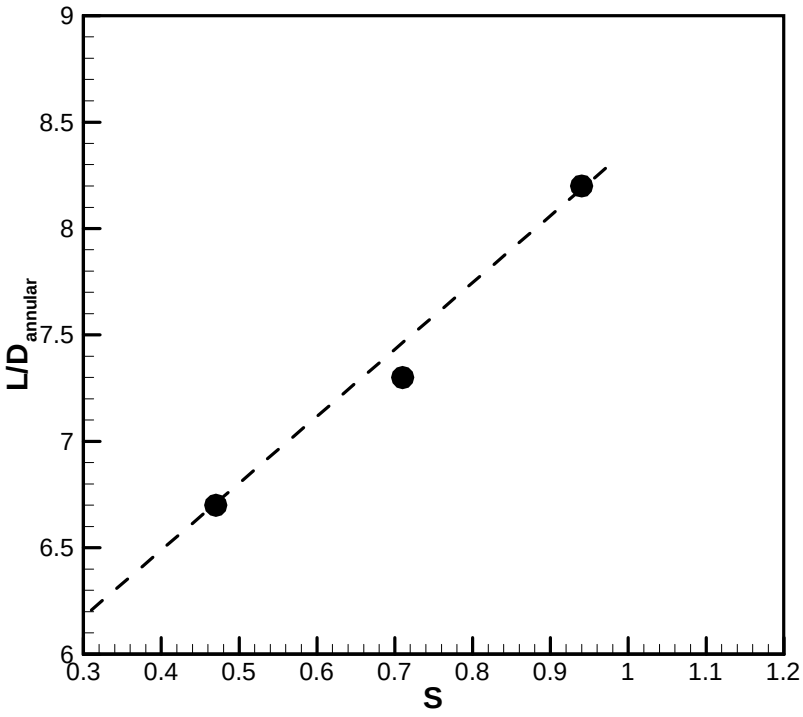

Fig. 17. Effect of S on axial length of the central recirculation zone

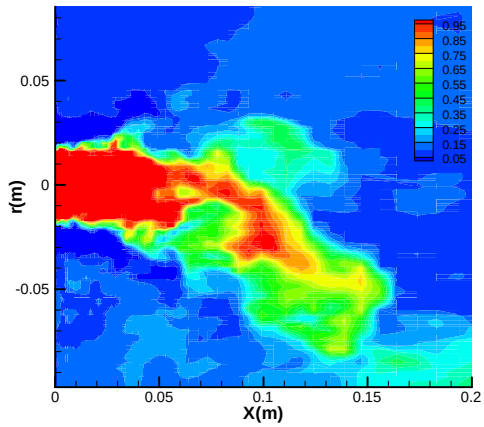

(a)

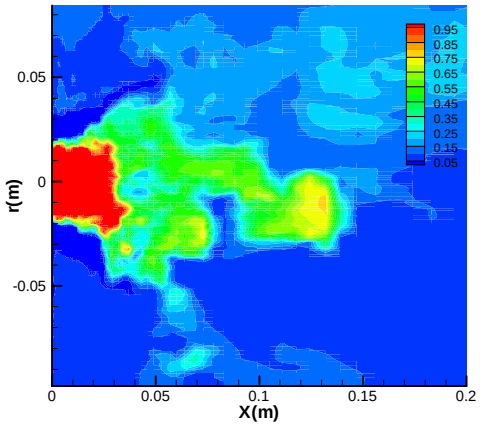

(b)

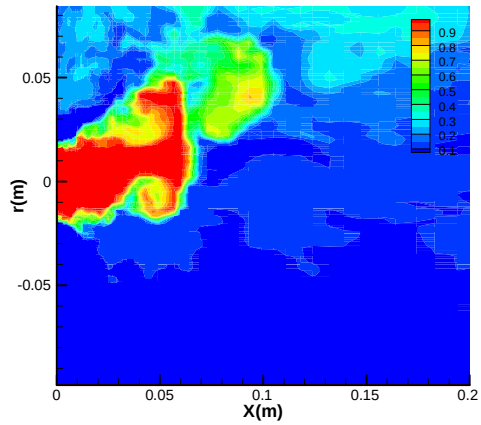

(c)

Fig. 18. Snapshots of passive scalar for case I (a), case II (b) and case III (c)

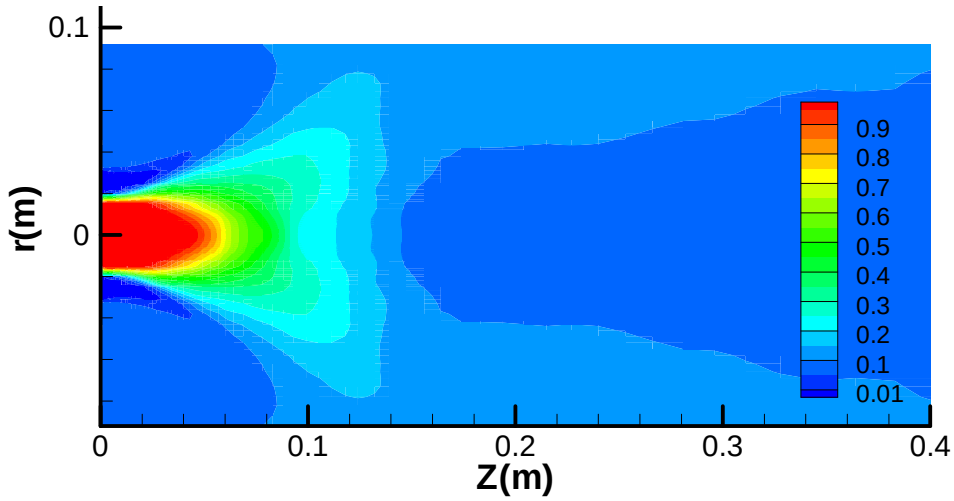

(a)

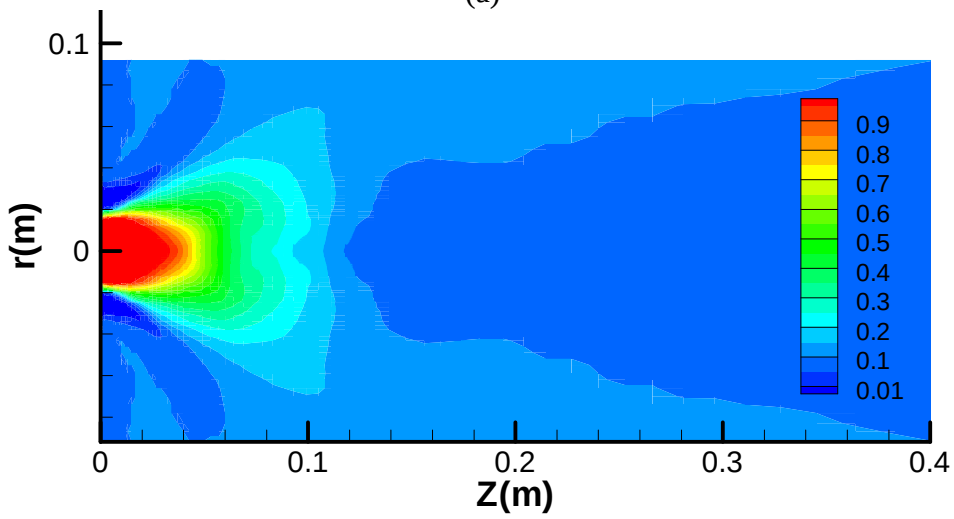

(b)

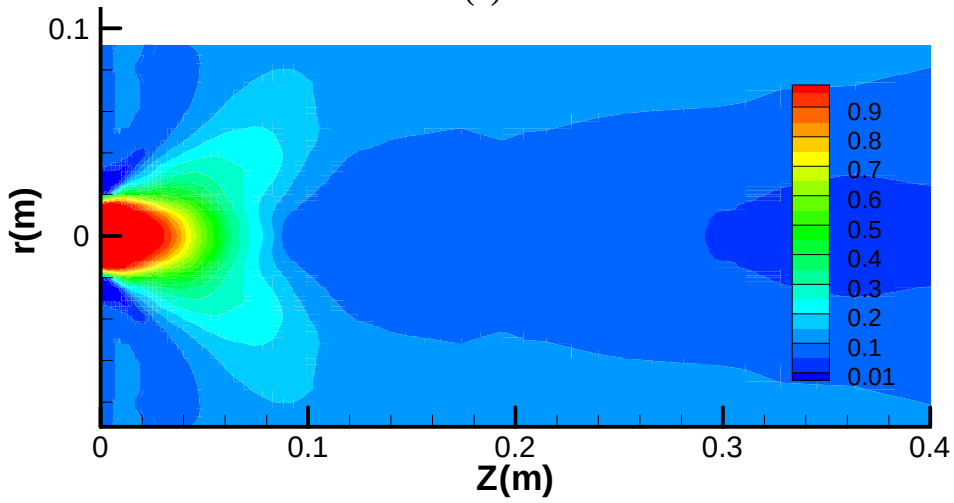

(c)

Fig. 19. Contour plots of mean passive scalar for case I (a), case II (b) and case III (c)

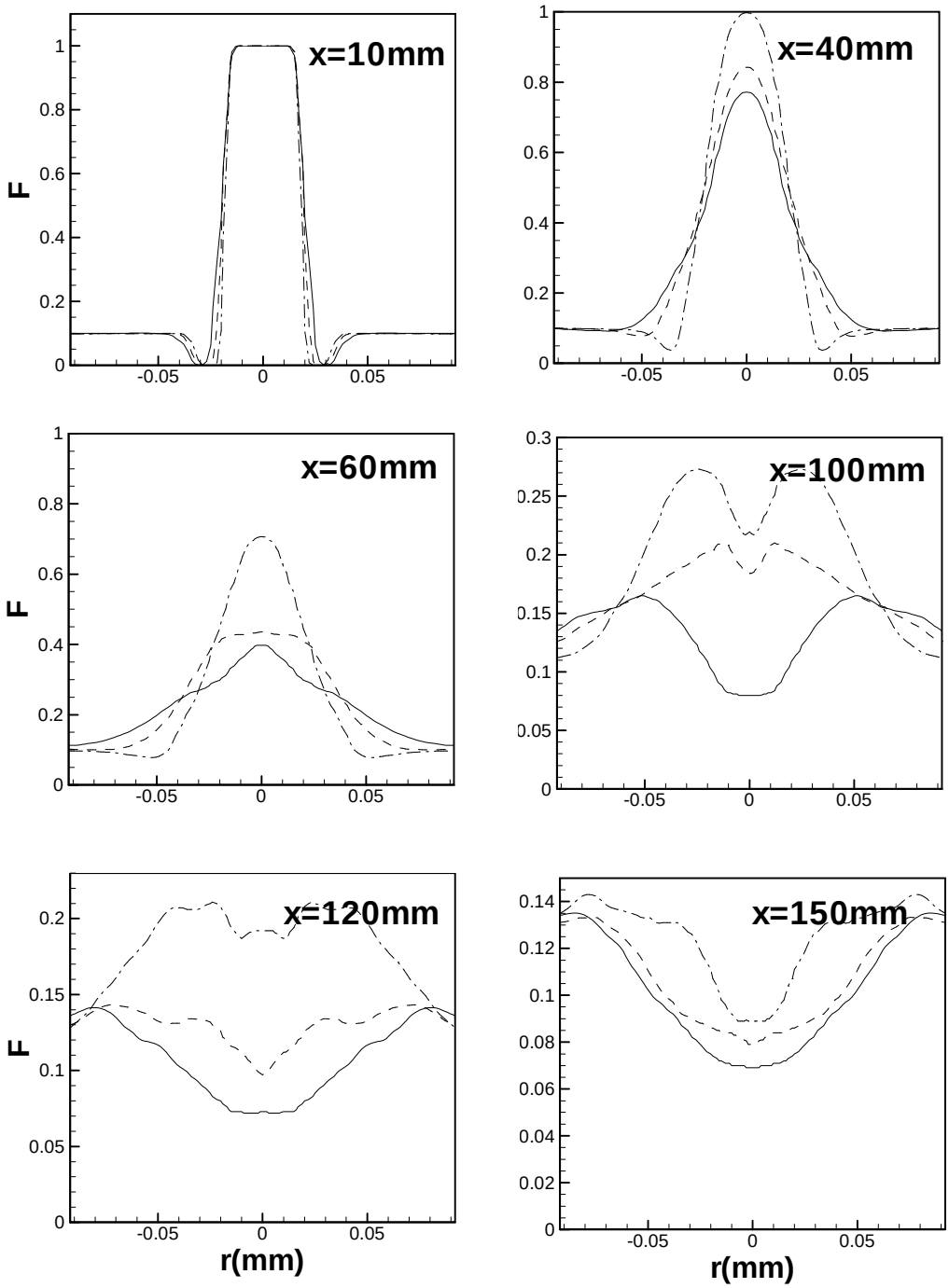

Fig. 20. Radial plots of time averaged mean passive scalar. Here dashed-dot-dashed line indicates case (I), dashed line indicates case II and solid line indicates case III results.

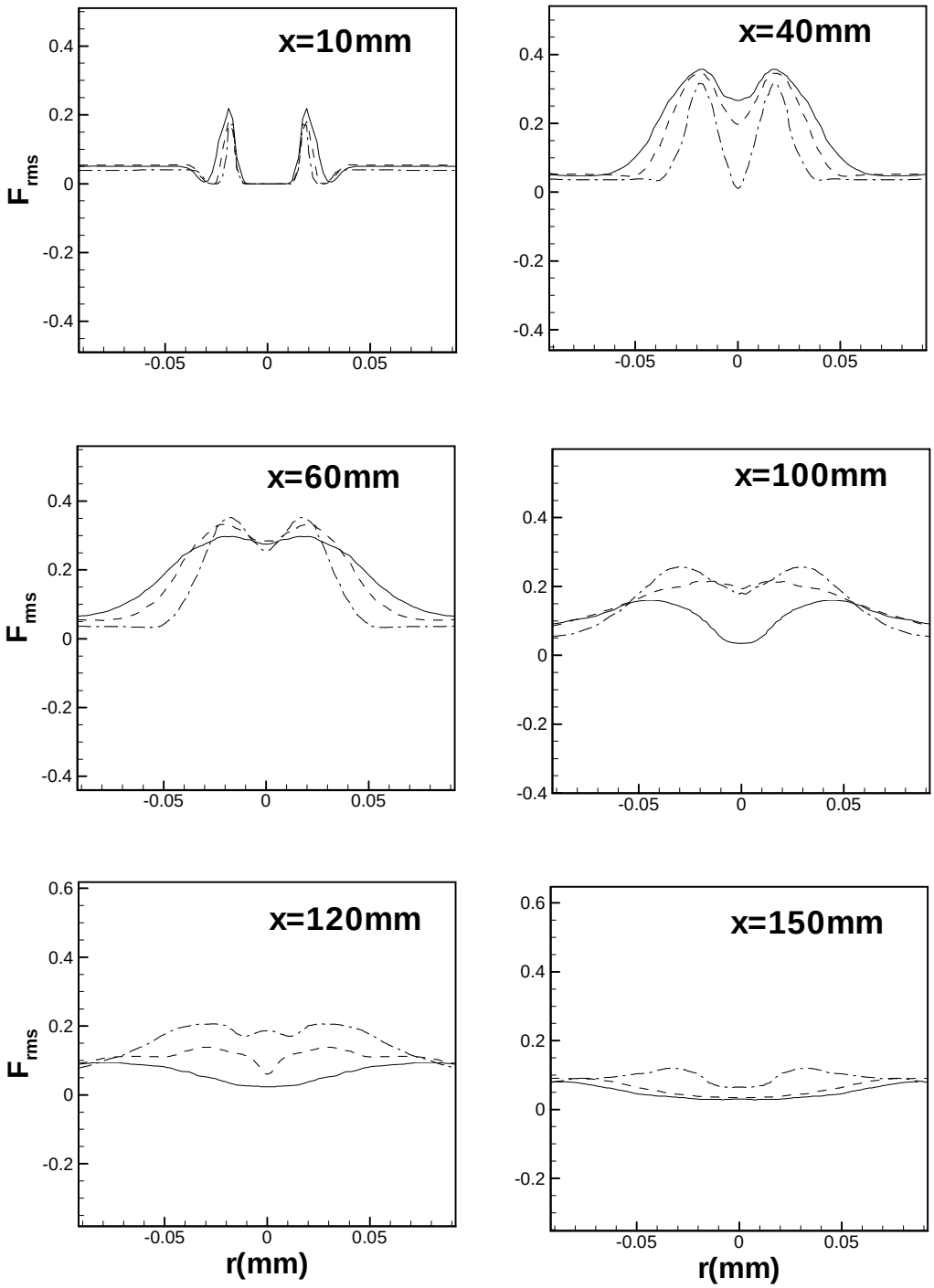

Fig. 21. Radial plots of time averaged passive scalar variance. Here dashed-dot-dashed line indicates case (I), dashed line indicates case II and solid line indicates case III results